



ELSEVIER

Available online at [www.sciencedirect.com](http://www.sciencedirect.com)

SCIENCE @ DIRECT®

Electronic Notes in Discrete Mathematics 20 (2005) 419–437

[www.elsevier.com/locate/ndm](http://www.elsevier.com/locate/ndm)

Electronic Notes in  
DISCRETE  
MATHEMATICS

# Resolving Ambiguities in Reconstructed Grain Maps using Discrete Tomography

A. Alpers<sup>a,1,3</sup> E. Knudsen<sup>b,2,4</sup> H.F. Poulsen<sup>b,2,4</sup>  
G.T. Herman<sup>a,1,3</sup>

<sup>a</sup> *Dept. of Computer Science, The Graduate Center, City University of New York,  
NY 10016, USA.*

<sup>b</sup> *Center for Fundamental Research: 'Metal Structures in Four Dimensions',  
Risø National Laboratory, DK-4000 Roskilde, Denmark.*

---

## Abstract

The so-called 3DXRD microscope, implemented at the European Synchrotron Radiation Facility in Grenoble, France, utilizes the principle of X-ray diffraction for mapping the crystalline grains within hard materials such as metals or ceramics. Present algorithms, using continuous models, roughly reconstruct the image from diffraction data, but they are often unable to assign unambiguous values to all pixels. We present an approach that resolves these ambiguous pixels by using a Monte Carlo technique that exploits the discrete nature of the problem and utilizes proven methods of discrete tomography. Based on simulations we show that most ambiguities can be successfully resolved.

*Keywords:* discrete tomography, polycrystals, crystallography, Gibbs distribution, X-ray diffraction, image restoration

---

<sup>1</sup> Partially supported by NIH grant HL70472 and NSF grant DMS0306215

<sup>2</sup> Partially supported by the Danish National Research Foundation

<sup>3</sup> Email: [awalpers@yahoo.de](mailto:awalpers@yahoo.de), Email: [gabortherman@yahoo.com](mailto:gabortherman@yahoo.com)

<sup>4</sup> Email: [erik.knudsen@risoe.dk](mailto:erik.knudsen@risoe.dk), Email: [henning.friis.poulsen@risoe.dk](mailto:henning.friis.poulsen@risoe.dk)

## 1 Introduction

Hard polycrystalline materials such as metals, alloys and most ceramics are widely used in industrial applications. Their physical, chemical and mechanical properties are to a large extent governed by the structure of the individual crystals inside. The study of these individual crystals, called *grains*, is an integral part of modern materials science.

Traditional grain map generation techniques are based on optical or electron microscopy, and thus only allow studies of surface structures. Three-dimensional maps could only be obtained by serial sectioning, i.e., by destructive techniques, whereas three-dimensional dynamic studies, such as studying processes of grain growth, were out of reach since they called for non-destructive techniques. Recently, such a technique based on X-ray diffraction has been developed at the Risø National Laboratory [8] and has been implemented at the three-dimensional X-ray diffraction (3DXRD) microscope at beamline ID11 of the European Synchrotron Radiation Facility (ESRF) in Grenoble.

The experimental geometry of the 3DXRD method can be roughly described as follows: One layer of a sample is illuminated by an incoming micro-focused high-energy X-ray beam. The sample itself is mounted on a rotation table, with rotation axis perpendicular to the illuminated plane. For some angles of rotation, some grains in this plane give rise to diffracted beams (according to *Bragg's law*) that are recorded on a two-dimensional detector. From the collection of these detector data the morphology of the grains in the layer has to be reconstructed. By stacking results from layers a 3D grain map can be obtained.

The forward problem (i.e., the calculation of the intensities on the detector for a single grain) can be stated as that of evaluating a linear function  $A_i x_i$ , where  $A_i$  is a real-valued matrix describing the diffraction geometry, and  $x_i$  is a 0/1-valued vector describing the characteristic function of the single grain  $g_i$ . The inverse problem (for a single grain) amounts to solving the linear system of equations  $A_i x_i = b_i$ , where  $b_i$  describes the measured data.

At present, the following method for grain map reconstruction is used [9]. A program called GRAINDEX, based on ray tracing, analyzes the diffraction spots on the detector and identifies those spots that can only originate from a single grain  $g_i$ . Data from these spots form the vector  $b_i$ , and then an Algebraic Reconstruction Technique (ART) [3] is applied to solve  $A_i x_i = b_i$ . But this solution is unlikely to be 0/1-valued, and is thus binarized by using a threshold. This procedure is carried out for each single grain separately and

provides reasonable results. But two (physical impossible) phenomena occur:

- (i) It happens that some pixels are assigned to two different grains.
- (ii) There are interior pixels that are assigned to no grains at all.

In this paper we discuss a method that tries to resolve these problems by taking the actual nature of the grain maps into account. Our approach is based on a *Markov-chain-based Monte Carlo method* [7] and uses Gibbs distribution for modeling a priori information [1], [6].

The paper is structured as follows: After a general description of our approach in Section 2 we formally introduce the utilized Gibbs priors in Section 3. Our results are given in Section 4, followed by our conclusions in Section 5. A detailed account of the basic crystallographic terms and a mathematical description of the data acquisition process is given in the Appendix.

## 2 Our Approach

The central idea of our approach is to take as input a 2D grain map  $f$  (generated by ART as described above) and the diffraction data. In the sequel we consider  $f$  to be a function defined on a finite domain  $D \subset \mathbb{Z}^2$  mapping into  $\{1, \dots, l\}$ ,  $l \in \mathbb{N}$ , the set representing the finite number of grains. In this sense, we are dealing with multi-colored images. Our proposed algorithm only changes pixels of the grain map that exhibit either of the properties (i) or (ii) above (referred to as *ambiguous pixels*). The task is to assign these pixels to the “correct” grain.

To this end we utilize a Markov-chain-based Monte Carlo method, namely the *Metropolis algorithm* [7], which has proved to be useful in other applications of Discrete Tomography, such as the reconstruction of binary (or gray-leveled) images from projections [4]. We assume that the grain maps are random samples from a *Gibbs distribution* defined by

$$(1) \quad \pi(f) = \frac{1}{Z} e^{-H(f)},$$

where  $\pi(f)$  is the probability of occurrence of the grain map  $f$ ,  $Z$  is the normalizing factor and  $H(f)$  the energy of  $f$ . This energy  $H(f)$  is based only on local  $3 \times 3$  features (called *configurations*) of the image, i.e.,

$$(2) \quad H(f) = - \sum_{c=1}^C N(G_c, f) U_c,$$

where  $N(G_c, f)$  counts the number of times a configuration  $G_c$  occurs in  $f$ , and the numbers  $U_1, \dots, U_C$  describe suitable Gibbs distribution parameters.

ters [6]. These parameters are chosen so that random samples resemble the arrangement of grains in polycrystals.

A single step of the Metropolis algorithm may be described as follows. One of the ambiguous pixels is randomly selected together with an alternative assignment of the pixel to a grain. Then, we calculate  $p = \frac{\pi(f')}{\pi(f)}$ , the ratio of the probabilities of the new grain map  $f'$  (which we would obtain if we assigned the pixel to the alternative grain) and the old grain map  $f$ . We accept this change with probability  $\min\{1, p\}$ . One *cycle* of the Metropolis algorithm consists of  $n$  Metropolis steps, where  $n$  is the total number of ambiguous pixels in the grain map.

However, this approach does not take the diffraction data  $P$  into account. (Such data can be modeled as a real-valued vector.) Let  $P_f$  denote the simulated diffraction data given the image  $f$ , and let  $\alpha, \beta \in \mathbb{R}$  be given positive parameters. We apply the Metropolis algorithm to the non-zero valued distribution  $\gamma$  defined by

$$(3) \quad \gamma(f) = \frac{1}{Z} e^{-\beta(H(f) + \alpha\|P_f - P\|_1)},$$

where  $\|\cdot\|_1$  denotes the  $\ell_1$ -norm. The reason for choosing  $\gamma$  as in (3) is that we want to find the grain map  $f$  that minimizes  $H(f) + \alpha\|P_f - P\|_1$ . This can be provided within an adequate running time by the Metropolis algorithm combined with an adequate annealing scheme for  $\beta$  [4]. The results that we present in Section 4 are obtained without annealing, instead we report the minimum that was found over a certain running time of the Metropolis algorithm. We decided in favour of this approach because the so obtained results had already a good quality. Only a minor improvement can be expected in this case by using more sophisticated optimization techniques such as Simulated Annealing.

Note that the data acquisition is similar to what is usual in discrete tomography, with the important difference that the diffraction spots do not correspond to measured sums along straight lines, but rather correspond to measured sums taken over more general sets. Our approach differs in this sense from approaches formerly known in the discrete tomography literature. Another difference to known approaches is that we are not dealing with Gibbs distributions defined on binary images but rather on multicolored images. But in order to keep the number of parameters low, we compute  $H(f)$  by suitably resorting to binary configurations, as will be explained in the next section.

### 3 Gibbs Priors for Grain Maps

In the following let

$$(4) \quad D = \{(i, j) \in \mathbb{Z}^2 \mid 0 \leq i < I, 0 \leq j < J\},$$

where  $I$  and  $J$  are positive integers, and  $\mathbb{Z}^2$  denotes the integer lattice. A grain map  $f$  is a function mapping  $D$  into a finite set  $\{1, \dots, l\}$  of integers. Every non-empty subset of  $D$  is called a *clique*. Given a clique  $q$ , a *configuration (over  $q$ )* is defined as a function  $g$  mapping from  $q$  into  $\{1, \dots, l\}$ . A *model* is a pair  $(Q, U)$  in which  $Q$  is a set of cliques and  $U$  is a function mapping the set of all possible configurations over all cliques in  $Q$  into the real numbers. The value of  $U(g)$  is called the *potential* of the configuration  $g$ . For a model  $\mu = (Q, U)$ , the  $\mu$ -energy of a grain map  $f$  is defined as

$$(5) \quad H_\mu(f) := - \sum_{q \in Q} U(f|q),$$

where  $f|q$  denotes the restriction of  $f$  to the clique  $q$ . The probability assigned to a grain map  $f$  is defined as in (1). Such a (suitably chosen) Gibbs distribution will serve as a prior in our approach. In order to obtain a computationally feasible prior we reduce the parameters involved in (5). One meaningful way to achieve this is to utilize  $3 \times 3$  cliques, i.e., by considering the domain  $D$  as in (4) we define

$$(6) \quad q_{(i,j)} := \{(i + \delta_i, j + \delta_j) \mid \delta_i, \delta_j \in \{-1, 0, 1\}\}, \text{ where } i, j \in \mathbb{Z}$$

and

$$(7) \quad Q := \{q_{(i,j)} \mid 1 \leq i < I - 1 \text{ and } 1 \leq j < J - 1\}.$$

Given a clique  $q_{(i,j)}$  and a configuration  $G_c : q_{(1,1)} \rightarrow \{1, \dots, l\}$ , we say  $f|q_{(i,j)} \sim G_c$  if and only if the following identities hold:  $f(i + \delta_1, j + \delta_2) = G_c(1 + \delta_1, 1 + \delta_2)$ , where  $\delta_1, \delta_2 \in \{-1, 0, 1\}$ . A 90-degree rotation of  $G_c$  is the configuration  $G_c^{90} : q_{(1,1)} \rightarrow \{1, \dots, l\}$  defined by  $G_c^{90}(i, j) = G_c(2 - j, i)$ ,  $i, j \in \{0, 1, 2\}$ . A horizontal reflection  $G_c^H : q_{(1,1)} \rightarrow \{1, \dots, l\}$  is defined by  $G_c^H(i, j) = G_c(2 - i, j)$ ,  $i, j \in \{0, 1, 2\}$ . A vertical reflection  $G_c^V : q_{(1,1)} \rightarrow \{1, \dots, l\}$  is defined by  $G_c^V(i, j) = G_c(i, 2 - j)$ ,  $i, j \in \{0, 1, 2\}$ .

Given a clique  $q_{(i,j)}$  and a configuration  $G_c : q_{(1,1)} \rightarrow \{1, \dots, l\}$  we say that  $f|q_{(i,j)} \equiv G_c$  if and only if there is a sequence of 90-degree rotations, horizontal and vertical reflections which applied to  $G_c$  gives a configuration  $G$  with  $f|q_{(i,j)} \sim G$ .

Further, let  $C$  initial configurations  $G_1, \dots, G_C : q_{(1,1)} \rightarrow \{0, \dots, l\}$  with potentials  $U(G_1|q_{(1,1)}) = U_1, \dots, U(G_C|q_{(1,1)}) = U_C$  be given. For  $q_{(i,j)}$  we

define

$$(8) \quad U(f|q_{(i,j)}) := \begin{cases} U_k & : f|q_{(i,j)} \equiv G_k \text{ for a } k \in \{1, \dots, C\}, \\ 0 & : \text{otherwise.} \end{cases}$$

In each step of the Metropolis algorithm we do not actually compute  $\pi(f)$  directly, but rather we compute the ratio of the probabilities of two images  $f$  and  $f'$  which differ in a single point  $d = (d_1, d_2) \in D$ . This ratio can be computed locally because the potentials of configurations defined on  $q_{(i,j)}$  with  $d \notin q_{(i,j)}$  are not affected by the pixel change. This means

$$(9) \quad \ln \left( \frac{\pi(f')}{\pi(f)} \right) = \sum_{(i,j) \in q(d_1, d_2)} (U(f'|q(i,j)) - U(f|q(i,j))).$$

Up to this point our model requires only the specification of  $C$  configurations  $G_1, \dots, G_C : q_{(1,1)} \rightarrow \{1, \dots, l\}$  and their potentials  $U_1, \dots, U_C$ . As we are dealing with multi-colored images (i.e.,  $l > 1$ ) we still have to take a great many of these configurations into account in order to obtain a useful model. This can be a problem because these configurations are usually stored in a lookup table. Therefore, we take a binary approach.

The multi-colored image  $f : D \rightarrow \{1, \dots, l\}$  can be decomposed into binary images  $f_i : D \rightarrow \{0, 1\}$ , where for every  $d \in D$  and  $i = 1, \dots, l$  we define

$$(10) \quad f_i(d) := \begin{cases} 1 & : \text{if } f(d) = i, \\ 0 & : \text{otherwise.} \end{cases}$$

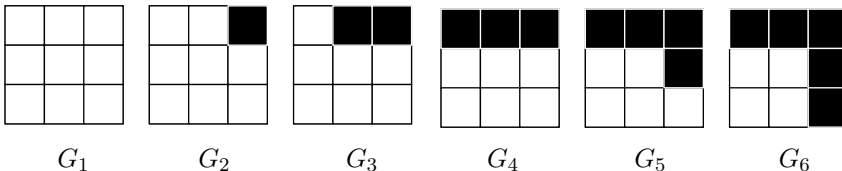


Fig. 1. The configurations  $G_1, \dots, G_6$  of a  $3 \times 3$  clique that we use in our model. The color of the boxes represent the value of the corresponding pixel: White boxes represent the value 1, black boxes represent the value 0.

Thus,  $f = \sum_{i=1}^l i f_i$ . By considering binary configurations  $G_1^b, \dots, G_C^b : D \rightarrow \{0, 1\}$  we only have to give (8) a different meaning, namely we redefine

$$(11) \quad U(f|q_{(i,j)}) := \begin{cases} U_k & : \text{ if } f_{f(i,j)}|q_{(i,j)} \equiv G_k^b \text{ for a } k \in \{1, \dots, C\}, \\ 0 & : \text{ otherwise.} \end{cases}$$

Another reason for the binary approach is that most of the  $3 \times 3$  subregions of a typical grain map contain at most two grains, and that the shape of any individual grain should not depend on its particular color (grain type).

In the following we will specify the configurations  $G_1, \dots, G_C : q_{(1,1)} \rightarrow \{0, 1\}$  that we use in “our model”. We distinguish between the  $C = 6$  basically different configurations  $G_1, \dots, G_C$  as depicted in Figure 1. In Section 4 we shall specify which potentials ( $U_1, U_2, U_3, U_4, U_5, U_6$ ) we actually used.

## 4 Results

Figure 2 shows one aluminum grain maps of  $128 \times 128$  pixel size containing 44 grains (left image), and its reconstruction using ART (right image). The right image contains 929 white pixels, which correspond to ambiguous points that ART was unable to reconstruct, even with noiseless detector data. Our approach tries to resolve the ambiguous white pixels, an ideal output of our algorithm would be the retrieval of the left image.

Taking the original image, we simulated noiseless detector data and ran our algorithm on the image with ambiguities using a 3.06 GHz Pentium 4 processor. Initially, the white points were randomly assigned to the grains that

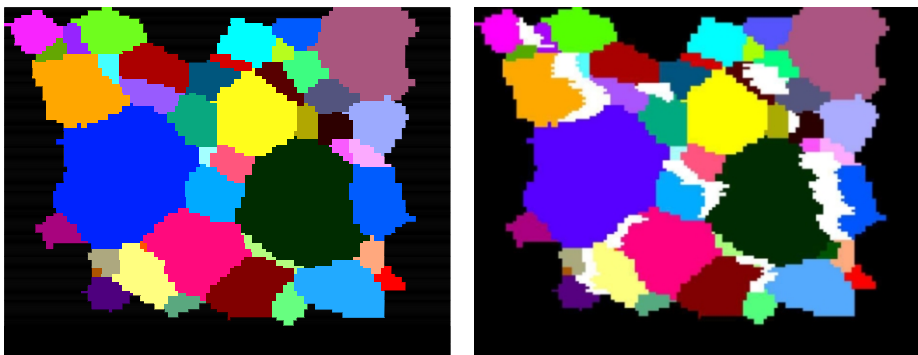


Fig. 2. The left image shows a typical grain map, which was experimentally determined by electron microscopy. The right image shows the grain map (produced by ART) where ambiguities have to be resolved (white points).

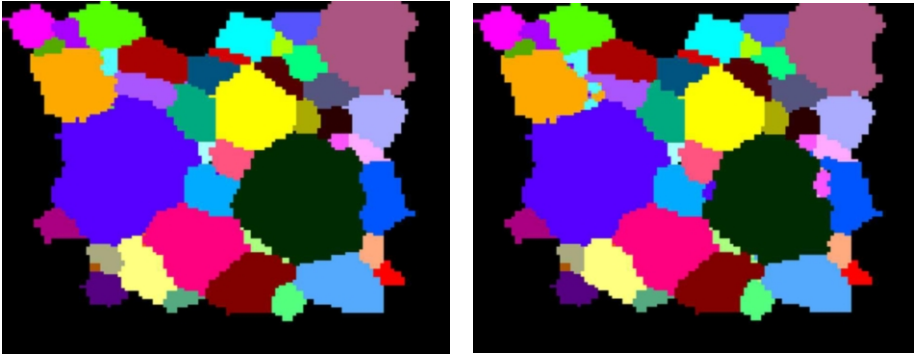


Fig. 3. Reconstruction using Gibbs priors and no projection data. The left image shows a sample obtained using the parameters  $U = (1.5; 1.2; 0.84; 1; 1.25; 0.6)$ , the right image is obtained by using the parameters  $U' = (1.2; 1.2; 0.84; 1; 1.25; 0.6)$ .

surround the white region in which they occurred. The size of the detector (in pixels) was  $1024 \times 1536$ , and we used 91 projections according to equally spaced rotation angles  $\omega$  between 0 and 90 degrees. In our simulations it turned out that only roughly one percent of all pixels on the detectors were actually hit by diffraction beams (thus having non-zero value), and most grains produced approximately 8 spots on the detector. Every diffracted beam recorded on the detector hits only one detector pixel and adds a uniform amount of value 1 to its intensity. After simulation of the projections the average detector pixel intensity is around 4.6.

Experiments show that approximately 99% of the ambiguous points are correctly resolved by running the Metropolis algorithm for 5 sec, using only the noiseless detector data (i.e., in (3) we set  $\alpha := \beta := 1$  and define  $H(f) := 0$  for all images  $f$ ). In the noisy case, however, we expect that the Gibbs priors essentially improve the quality of the reconstruction. In this section we give results supporting this hypothesis.

We used three different sets of Gibbs parameters for our model (cf. Figure 1), namely  $U = (U_1; U_2; U_3; U_4; U_5; U_6) = (1.5; 1.2; 0.84; 1; 1.25; 0.6)$ ,  $U' = (1.2; 1.2; 0.84; 1; 1.25; 0.6)$  and  $\tilde{U} = (0.5; 0.4; 1.0; 0.8; 0.1; 0.6)$ . Notice that  $U$  and  $U'$  only differ in the value which is given for “uniform regions”. Running the Metropolis algorithm using only the Gibbs priors  $U$  or  $U'$  (i.e. no projection at all) resulted in “grain-like” features (see Figure 3), with the only apparent difference that the parameters of  $U$  tended to fill up the white points with bigger sized grains. Based on this finding we chose these particular parameters, because they seemed to model a priori knowledge about grain shapes

quite adequately. The parameters  $\tilde{U}$ , however, were chosen arbitrarily in the sense that they do not obviously model any reasonable prior information.

Most of the following diagrams report on results with noisy projection data, stated in terms of how many pixels are affected by noise. This means that, for each of the 91 detector planes of size  $1024 \times 1536$ , we ran a loop for a fixed number of iterations where we randomly <sup>5</sup> selected a point on the detector and increased its intensity by 1. Different noise levels are shown in the diagrams as percentages normalized by the number of pixels on the detector. A noise level of 200%, e.g., means that on every detector plane we  $2 \cdot 1024 \cdot 1536$  times increased a pixel intensity by 1 (at random positions).

The  $y$ -axis of the following diagrams depicts the number of incorrectly reconstructed pixels (out of the total of 929 pixels). Unless stated otherwise we run the Metropolis algorithm for 5 sec (corresponding to 1,000 cycles). Each simulation was carried out 10 times, and each point in the diagrams correspond to the average value taken over these 10 runs.

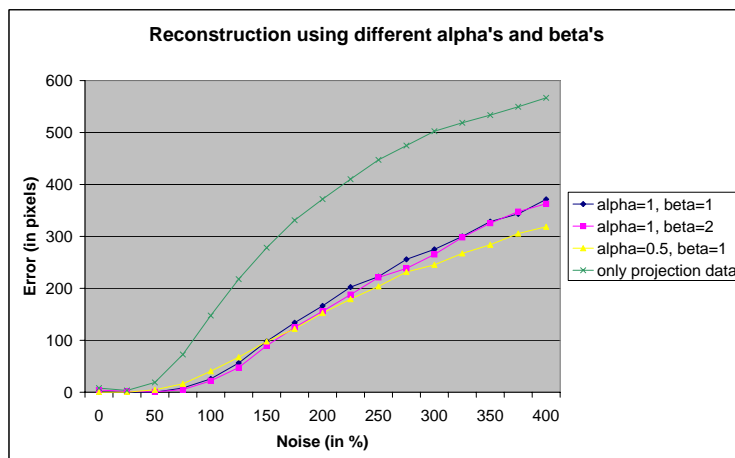


Fig. 4. Reconstruction using different  $\alpha$ 's and  $\beta$ 's. Noise level is shown in terms of how many detector pixel intensities were increased by 1.

Figure 4 shows four curves. The green curve was obtained without using a Gibbs prior, i.e.,  $\gamma(f) = \frac{1}{2}e^{-\beta(\alpha\|P_f - P\|_1)}$  in (3), and  $\alpha = \beta = 1$ . The other

<sup>5</sup> We picked the  $x$  and  $y$  coordinates from a uniform distribution.

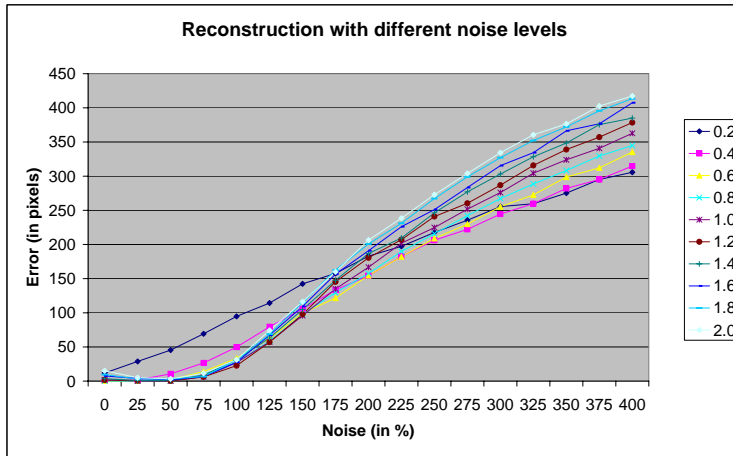


Fig. 5. Reconstruction using different  $\alpha$ 's and noise levels (Gibbs parameters  $U$ ).

curves were obtained by taking the Gibbs parameters  $U$  and the indicated values of  $\alpha$  and  $\beta$ . The figure shows that the projection data are, even in the noisy case, quite reliable. Combining projection data with Gibbs priors gives an improvement of the quality of the reconstruction. At high noise levels, approximately twice as many pixels were reconstructed correctly with a Gibbs prior than without a Gibbs prior. Additionally, the figure indicates that the reconstruction is not sensitive to the  $\beta$  values, which is promising because this parameter has to be chosen empirically.

Figure 5 shows results for different noise levels, where for reconstruction we used the Gibbs parameters  $U$  and  $\beta = 1$ . Different curves correspond to different values of  $\alpha$ .

Figure 6 matches Figure 5, except that we used the Gibbs parameters  $U'$ . On the one hand, the figure shows that as the level of noise increases one should decrease  $\alpha$  to obtain good reconstructions. On the other hand, the results obtained with the Gibbs parameters  $U$  have a better quality than the corresponding results with  $U'$ . This shows that choosing meaningful Gibbs parameters really improves the quality of reconstruction.

For the simulations depicted in Figure 7, we fixed  $\alpha = 0.2$ ,  $\beta = 1$ ,  $U$  and chose a noise level of 200%. We created 10 test sets of noisy projection data

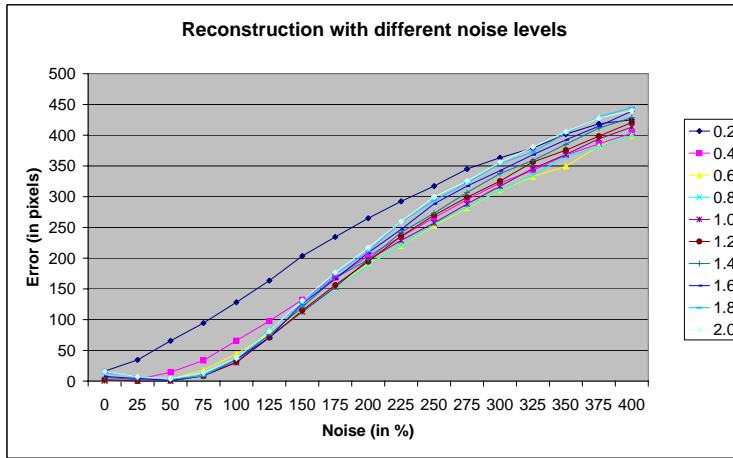


Fig. 6. Reconstruction using different  $\alpha$ 's and noise levels (Gibbs parameters  $U'$ ).

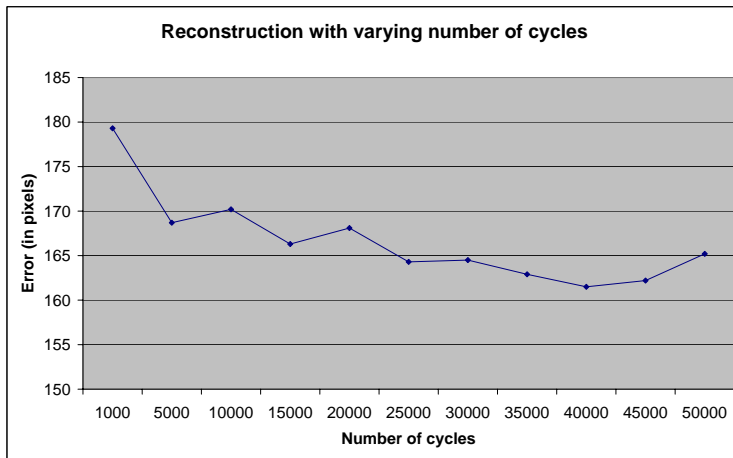


Fig. 7. Reconstruction with different cycles.

and stopped the algorithm after a certain number of cycles (as shown in the diagram). It can be seen that a longer running time gives better results.

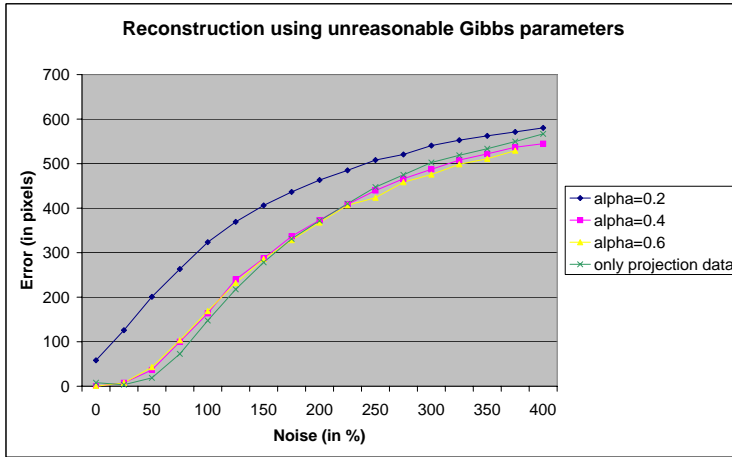


Fig. 8. Reconstruction with arbitrary Gibbs parameters  $\hat{U}$ .

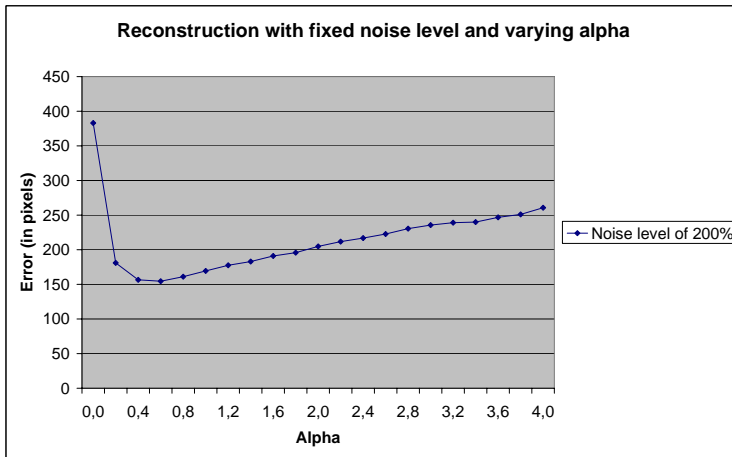


Fig. 9. Reconstruction with fixed noise level of 200% and varying  $\alpha$ .

Figure 8 shows the outcome of some simulations with  $\beta = 1$  and  $\hat{U}$ . The curves correspond to different values of  $\alpha$ . As the parameters  $\hat{U}$  were chosen

quite arbitrarily, we can see in the figure that the reconstruction quality is worse compared to other parameters (cf. Figure 5). However, they are still better compared to the case using only projection data (cf. Figure 4).

Figure 9 shows results when we fixed the noise level at 200% and used parameters  $U$  and  $\beta = 1$ . The curve shows the reconstruction results for varying values of  $\alpha$ . The optimal value for this noise level seems to lie around  $\alpha = 0.4$ .

Finally, in Figure 10 we repeated the same simulations as shown in Figure 9, but this time we fixed the noise level to 50%. It can be seen that the optimal value for  $\alpha$  is now around  $\alpha = 1.0$ .

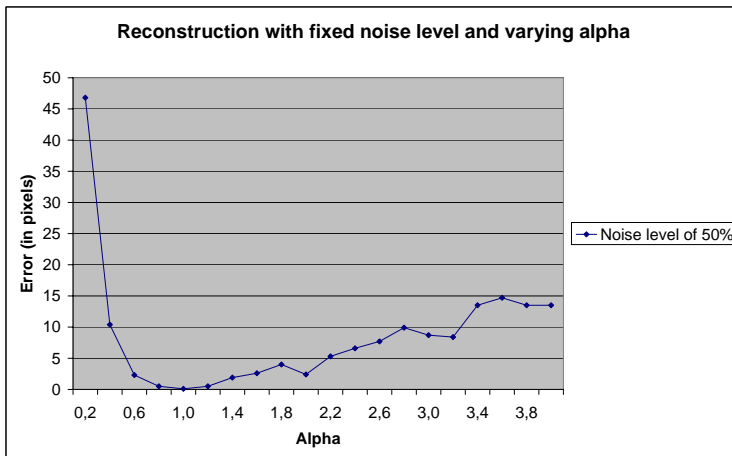


Fig. 10. Reconstruction with fixed noise level of 50% and varying  $\alpha$ .

## 5 Conclusions

We have introduced a new approach, based on methods from Discrete Tomography, to improve the quality of reconstructed grain maps obtained from diffraction data. Based on simulations we have shown that a large number of ambiguous points can be resolved successfully. The noise in experimental 3DXRD data is estimated to be at most 100%. It appears from Figure 4 that in this low noise range, the use of Gibbs priors reduces the error of the reconstruction by a factor of about 5. Moreover, we have discussed the influence

of different parameters of the model showing the degree of robustness of our approach.

Further improvements are expected by applying an annealing scheme, a longer running time of the algorithm, optimizing the parameters of the Gibbs priors, and by selecting the optimal  $\alpha$  according to the noise level in experimental data. Finally, we plan to carry out extensive tests with experimental data.

## 6 Appendix

This appendix gives a brief introduction to the crystallographic notions relevant for this paper. Furthermore, the mathematical relationship between the object and its projections is explained (following [5], [8]). For a deeper introduction we refer to [10].

### 6.1 Lattices

A polycrystal, as mentioned in the introduction, consists of smaller crystals (grains) at different orientations. The crystal's regularity, i.e., the periodic array in which the repeated units of the crystal are arranged, is captured by the concept of the *Bravais lattice*. This (three-dimensional) lattice is the set

$$(12) \quad \mathcal{L} = \{\mathbf{x} \in \mathbb{R}^3 \mid \mathbf{x} = \alpha_1 \mathbf{a} + \alpha_2 \mathbf{b} + \alpha_3 \mathbf{c}, \alpha_1, \alpha_2, \alpha_3 \in \mathbb{Z}\},$$

where  $\mathbf{a}, \mathbf{b}, \mathbf{c} \in \mathbb{R}^3$  are given vectors not all lying in the same plane. The vectors  $\mathbf{a}, \mathbf{b}$  and  $\mathbf{c}$  are called the *primitive vectors*. Aluminum, the material that we used for our simulations, forms a face-centered cubic Bravais lattice that is obtained by (12) with  $\mathbf{a} = \frac{1}{2}(0, 1, 1)^T$ ,  $\mathbf{b} = \frac{1}{2}(1, 0, 1)^T$  and  $\mathbf{c} = \frac{1}{2}(1, 1, 0)^T$ . In the crystallographic literature, one often specifies a lattice by six *lattice parameters*  $(a, b, c, \alpha, \beta, \gamma) \in \mathbb{R}^6$ . These parameters define the lengths of the primitive vectors and their interaxial angles, i.e.,

$$(13) \quad a = \|\mathbf{a}\|, b = \|\mathbf{b}\|, c = \|\mathbf{c}\|$$

and

$$(14) \quad \alpha = \arccos \frac{\langle \mathbf{b}, \mathbf{c} \rangle}{bc}, \beta = \arccos \frac{\langle \mathbf{c}, \mathbf{a} \rangle}{ca}, \gamma = \arccos \frac{\langle \mathbf{a}, \mathbf{b} \rangle}{ab}.$$

Polycrystals containing two grains with different lattice structure are said to be in *multiphase*, otherwise they are in *monophase*. It is this latter case that we consider in this paper.

Given a Bravais lattice with primitive vectors  $\mathbf{a}, \mathbf{b}$  and  $\mathbf{c}$  one defines the reciprocal lattice to be the lattice with primitive vectors  $\mathbf{a}^*, \mathbf{b}^*$  and  $\mathbf{c}^*$  fulfilling

$$(15) \quad \langle \mathbf{a}, \mathbf{a}^* \rangle = \langle \mathbf{b}, \mathbf{b}^* \rangle = \langle \mathbf{c}, \mathbf{c}^* \rangle = 2\pi$$

and

$$(16) \quad \langle \mathbf{a}, \mathbf{b}^* \rangle = \langle \mathbf{a}, \mathbf{c}^* \rangle = \langle \mathbf{b}, \mathbf{a}^* \rangle = \langle \mathbf{b}, \mathbf{c}^* \rangle = \langle \mathbf{c}, \mathbf{a}^* \rangle = \langle \mathbf{c}, \mathbf{b}^* \rangle = 0$$

where  $\langle \cdot \rangle$  denotes the scalar product.

*Lattice planes* (defined as planes containing at least three noncollinear Bravais lattice points) are an essential notion for describing the diffraction process. These lattice planes are usually described by *Miller indices*, which are integers  $h, k, l \in \mathbb{Z}$ , with greatest common divisor equal to 1, defining the lattice plane normal to the vector  $h\mathbf{a}^* + k\mathbf{b}^* + l\mathbf{c}^*$  in the reciprocal lattice.

The orientation of a grain can be described by a rotation in 3D space. Given a fixed coordinate system it is well known that such a rotation can be described by three angles  $(\psi, \varphi_1, \varphi_2)$ , the so called *Euler angles* [2]. In this notation, the first rotation is by an angle  $\psi$  about the z-axis, the second is by an angle about  $\varphi_1 \in [0, \pi]$  the x-axis, and the third is by an angle  $\varphi_2$  again about the z-axis (all angles measured anticlockwise). Straightforward calculations of the three rotation matrices yields the orientation matrix

$$(17) \quad \mathbf{U} = \begin{pmatrix} U_{11} & U_{12} & U_{13} \\ U_{21} & U_{22} & U_{23} \\ U_{31} & U_{32} & U_{33} \end{pmatrix},$$

where

$$(18) \quad \begin{aligned} U_{11} &= \cos(\varphi_1) \cos(\varphi_2) - \sin(\varphi_1) \sin(\varphi_2) \cos(\psi), \\ U_{12} &= -\cos(\varphi_1) \sin(\varphi_2) - \sin(\varphi_1) \cos(\varphi_2) \cos(\psi), \\ U_{13} &= \sin(\varphi_1) \sin(\psi), \\ U_{21} &= \sin(\varphi_1) \cos(\varphi_2) + \cos(\varphi_1) \sin(\varphi_2) \cos(\psi), \\ U_{22} &= -\sin(\varphi_1) \sin(\varphi_2) + \cos(\varphi_1) \cos(\varphi_2) \cos(\psi), \\ U_{23} &= -\cos(\varphi_1) \sin(\psi), \\ U_{31} &= \sin(\varphi_2) \sin(\psi), \\ U_{32} &= \cos(\varphi_2) \sin(\psi), \\ U_{33} &= \cos(\psi). \end{aligned}$$

### 6.2 Diffraction

The physical principle that governs the data acquisition process of the 3DXRD microscope is the principle of X-ray diffraction [8]. Diffraction spots on the detector appear if X-ray beams reflected on parallel lattice planes interfere constructively. *Bragg's law* states that the condition for scattering for a wave of wavelength  $\lambda$  against a series of lattice planes with lattice spacing  $d$ , rotated the angle  $\theta$  off the lattice plane normal, is

$$(19) \quad n\lambda = 2d \sin(\theta), \text{ for an } n \in \mathbb{N}.$$

Reformulated in terms of the scattering vector  $\mathbf{G}$  (defined as the difference between the vector describing the incident beam and the reflected beam, normalized so that  $|\mathbf{G}| = 2\pi/d$ ) Bragg's law states:

$$(20) \quad |\mathbf{G}| = \frac{4\pi}{n\lambda} \sin(\theta).$$

For a given set of Miller indices only the case  $n = 1$  is relevant, as any higher order harmonics is equivalent to an  $n = 1$  case for another distinct set of Miller indices. E.g., the  $n = 3$  case for (111) is equivalent to  $n = 1$  for (333).

### 6.3 Calculating Diffraction Spots

We use three Cartesian coordinate systems: the laboratory system, the rotation table system and the Cartesian grain system.

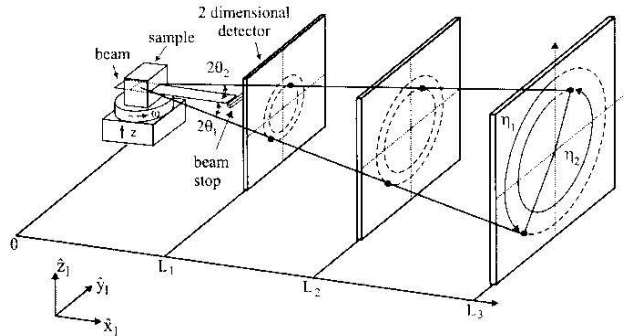


Fig. 11. Sketch of the 3DXRD geometry. Detectors are positioned perpendicular to the beam at distance  $L_1$ ,  $L_2$  and  $L_3$ .

The origins of the laboratory system and the rotation table coincide, and positive  $\omega$  values are measured according to Figure 11.

Let  $(\mathbf{x}_c, \mathbf{y}_c, \mathbf{z}_c)$  denote the Cartesian grain system which is fixed with respect to the reciprocal lattice  $(\mathbf{a}^*, \mathbf{b}^*, \mathbf{c}^*)$  in the grain.

Let  $\mathbf{G}_{\mathbf{hkl}}$  denote a scattering vector represented by the Miller indices in the reciprocal-lattice system. The correspondence between the Cartesian grain system and reciprocal space is given by the matrix  $B$ :  $\mathbf{G}_c = \mathbf{B}\mathbf{G}_{\mathbf{hkl}}$ , with

$$(21) \quad \mathbf{B} = \begin{pmatrix} a^* b^* \cos(\gamma^*) & c^* \cos(\beta^*) \\ 0 & b^* \sin(\gamma^*) - c^* \sin(\beta^*) \cos(\alpha) \\ 0 & 0 & c^* \sin(\beta^*) \sin(\alpha) \end{pmatrix}$$

and

$$(22) \quad \cos(\alpha) = \frac{\cos(\beta^*) \cos(\gamma^*) - \cos(\alpha^*)}{\sin(\gamma^*) \sin(\beta^*)}.$$

Here  $(a, b, c, \alpha, \beta, \gamma)$  and  $(a^*, b^*, c^*, \alpha^*, \beta^*, \gamma^*)$  symbolize the lattice parameters in direct and reciprocal space, respectively.

Given the orientation of the grain by the Euler angles  $(\psi, \varphi_1, \varphi_2)$ , this scattering vector further transforms by applying the orientation matrix  $\mathbf{U}$  of (17). Finally, taking the rotation by an angle  $\omega$  on the rotation table into account, we derive the representation in the laboratory system by

$$(23) \quad \mathbf{G}_1 = \Omega \mathbf{U} \mathbf{B} \mathbf{G}_{\mathbf{hkl}},$$

where

$$(24) \quad \Omega = \begin{pmatrix} \cos(\omega) & -\sin(\omega) & 0 \\ \sin(\omega) & \cos(\omega) & 0 \\ 0 & 0 & 1 \end{pmatrix}.$$

Given the angles  $\theta$  and  $\eta$  as in Figure 11 we deduce that

$$(25) \quad \mathbf{G}_1 = \frac{2\pi}{\sqrt{2 - 2 \cos(2\theta)}} \begin{pmatrix} \cos(2\theta) - 1 \\ -\sin(2\theta) \sin(\eta) \\ \sin(2\theta) \cos(\eta) \end{pmatrix}$$

Notice that  $\mathbf{G}_1$  is the diffraction vector, i.e., it is derived by subtracting the incoming beam vector from the diffracted beam vector (in polar coordinates).

Together with Bragg's law (20) we derive

$$(26) \quad \mathbf{G}_1 = \frac{2\pi}{\lambda} \begin{pmatrix} \cos(2\theta) - 1 \\ -\sin(2\theta) \sin(\eta) \\ \sin(2\theta) \cos(\eta) \end{pmatrix}$$

In summary, given a lattice plane we can calculate by (26) the angles  $\eta$  and  $\theta$  fulfilling Bragg's law, and thus infer that the beam is diffracted along a straight line with direction vector

$$(27) \quad \mathbf{V}_l = \begin{pmatrix} \cos(2\theta) \\ -\sin(2\theta) \sin(\eta) \\ \sin(2\theta) \cos(\eta) \end{pmatrix}.$$

Now, let  $(y_{det}(0), z_{det}(0))$  denote the intersection of the detector plane with the incoming (non-diffracted) ray passing through the origin of the laboratory system. Given a point  $(x_l, y_l, z_l)$  of the grain (with respect to the laboratory system), it easily follows that the associated diffraction point on the detector  $(L_1, y_{et}, z_{det})$  can be calculated by

$$(28) \quad \begin{aligned} y_{det} &= -(L_1 - x_l) \tan(2\theta) \sin(\eta) + y_l - y_{det}(0) \\ z_{det} &= (L_1 - x_l) \tan(2\theta) \cos(\eta) + z_l - z_{det}(0). \end{aligned}$$

## Acknowledgments

The authors would like to thank H.Y. Liao, L. Rodek and S.W. Rowland for many helpful discussions.

## References

- [1] Brémaud, P., "Markov Chains: Gibbs Fields, Monte Carlo Simulations, and Queues," Springer, New York, 1999.
- [2] Bunge, H. J., "Texture Analysis in Materials Science," Butterworths, London, 1982.
- [3] Gordon, R., R. Bender, and G. T. Herman, *Algebraic reconstruction techniques (ART) for three-dimensional electron microscopy and X-ray photography*, J. Theor. Biol. **29** (1970), 471–482.

- [4] Herman, G. T., and A. Kuba (Eds.), “Discrete Tomography: Foundations, Algorithms and Applications,” Birkhäuser, Boston, 1999.
- [5] Lauridsen, E. M., S. Schmidt, R. M. Auter, and H. F. Poulsen, *Tracking: A method for structural characterization of grains in powders or polycrystals*, *J. Appl. Cryst.* **34** (2001), 744–750.
- [6] Liao, H. Y., and G. T. Herman, *Automated estimation of the parameters of Gibbs priors to be used in binary tomography*, *Discrete Appl. Math.* **139** (2004), 149–170.
- [7] Metropolis, N., A. W. Rosenbluth, M. N. Rosenbluth, A. H. Teller, and E. Teller, *Equations of state calculations by fast computing machines*, *J. Chem. Phys.* **21** (1953), 1087–1092.
- [8] Poulsen, H. F., “Three-Dimensional X-ray Diffraction Microscopy: Mapping Polycrystals and their Dynamics,” Springer, Berlin, 2004.
- [9] Poulsen, H. F., and X. Fu, *Generation of grain maps by an algebraic reconstruction technique*, *J. Appl. Cryst.* **36** (2003), 1062–1068.
- [10] Warren, B. E., “X-Ray Diffraction,” Dover Publication, New York, 1990.